Stratospheric Temperature Trends over 1979–2015 Derived from Combined SSU, MLS, and SABER Satellite Observations

WILLIAM J. RANDEL, ANNE K. SMITH, AND FEI WU

National Center for Atmospheric Research, Boulder, Colorado*

CHENG-ZHI ZOU

Center for Satellite Applications and Research, NOAA/NESDIS, College Park, Maryland

HAIFENG QIAN

Earth Resource Technology, Inc., Laurel, Maryland

(Manuscript received 3 September 2015, in final form 30 March 2016)

ABSTRACT

Temperature trends in the middle and upper stratosphere are evaluated using measurements from the Stratospheric Sounding Unit (SSU), combined with data from the *Aura* Microwave Limb Sounder (MLS) and Sounding of the Atmosphere Using Broadband Emission Radiometry (SABER) instruments. Data from MLS and SABER are vertically integrated to approximate the SSU weighting functions and combined with SSU to provide a data record spanning 1979–2015. Vertical integrals are calculated using empirically derived Gaussian weighting functions, which provide improved agreement with high-latitude SSU measurements compared to previously derived weighting functions. These merged SSU data are used to evaluate decadal-scale trends, solar cycle variations, and volcanic effects from the lower to the upper stratosphere. Episodic warming is observed following the volcanic eruptions of El Chichón (1982) and Mt. Pinatubo (1991), focused in the tropics in the lower stratosphere and in high latitudes in the middle and upper stratosphere. Solar cycle variations are centered in the tropics, increasing in amplitude from the lower to the upper stratosphere. Linear trends over 1979–2015 show that cooling increases with altitude from the lower stratosphere (from ~ -0.1 to -0.2 K decade^{-1}) to the middle and upper stratosphere (from ~ -0.5 to -0.6 K decade^{-1}). Cooling in the middle and upper stratosphere is relatively uniform in latitudes north of about 30°S, but trends decrease to near zero over the Antarctic. Mid- and upper-stratospheric temperatures show larger cooling over the first half of the data record (1979–97) compared to the second half (1998–2015), reflecting differences in upper-stratospheric ozone trends between these periods.

1. Introduction

The temperature of the stratosphere has decreased over the last several decades because of the combined effects of increases in well-mixed greenhouse gases (GHGs) and changes in stratospheric ozone. Long-term cooling has been found in a number of observational datasets, including radiosonde, satellite, and ground-based lidar measurements (see reviews in Ramaswamy et al. 2001; Randel et al. 2009; Seidel et al. 2011). In the lower stratosphere, there is reasonable agreement in temperature trends derived from radiosonde and satellite datasets, in particular for satellite measurements from the Microwave Sounding Unit (MSU) (e.g., Seidel et al. 2011; WMO 2014). In contrast, there has been more uncertainty for temperature changes in the middle and upper stratosphere, where radiosonde data are unavailable and estimates rely primarily on merged operational satellite data (Thompson et al. 2012).

The primary dataset for estimating decadal-scale temperature trends in the middle and upper stratosphere is derived from the Stratospheric Sounding Unit (SSU). The SSU data are obtained from a series of different instruments on NOAA operational satellites that were intended for meteorological measurements, not for obtaining long-term climate-quality data. Creation of a

* The National Center for Atmospheric Research is sponsored by the National Science Foundation.

Corresponding author address: William Randel, National Center for Atmospheric Research, 3450 Mitchell Lane, Boulder, CO 80301.
E-mail: randel@ucar.edu

DOI: 10.1175/JCLI-D-15-0629.1

long-term climate data record from SSU requires merging measurements from the separate instruments and making corrections for a number of aspects such as instrument cell pressure changes, orbital drifts, increasing atmospheric CO_2, and other factors. At present two groups have undertaken the generation of climate data records from SSU: the Met Office (Nash and Saunders 2015) and the NOAA Center for Satellite Applications and Research (STAR) group (Wang et al. 2012; Zou et al. 2014). Thompson et al. (2012) compared SSU data from the so-called version 1 of the Met Office and NOAA SSU datasets, showing large differences in long-term trends between these data. Subsequently, both the Met Office and NOAA groups have produced revised and improved SSU datasets (version 2), and while there are still nontrivial differences between the two, there is substantially better agreement than for version 1 (Seidel et al. 2016). Overall, the adjustments required to produce a climate-quality data record from SSU measurements are much better understood than previously, and version 2 of the merged data is a substantially improved product.

The SSU data record began in late 1978 and ended in April 2006, when the last SSU instrument ceased operation. The objective of this paper is to extend the SSU data record to near present by combining with the more recent measurements from the *Aura* Microwave Limb Sounder (MLS; beginning in 2004) and Sounding of the Atmosphere Using Broadband Emission Radiometry (SABER; beginning in 2002). We vertically integrate the measurements from MLS and SABER to approximate the broad-layer SSU measurements and then combine the datasets based on the available overlap periods. This provides updated SSU-equivalent data records spanning 1979–2015, effectively extending the original SSU record by nearly a decade. Our work expands the results of Seidel et al. (2016), who focus on variability and trends in SSU data through the end of the record in 2006.

Our analyses complement the recent work of McLandress et al. (2015), who extend the SSU record using a combination of Advanced Microwave Sounding Unit (AMSU) and Michelson Interferometer for Passive Atmospheric Sounding (MIPAS) measurements, but are distinct in several ways. First, we utilize the direct overlap of SSU with MLS and SABER data (both of which cover the vertical range sampled by SSU) to merge and extend the SSU record. McLandress et al. (2015) utilize linear combinations of AMSU measurements to approximate the SSU weighting functions; this works well for SSU channels 1 and 2, but there are more uncertainties for SSU channel 3, which extends above the uppermost AMSU channel. McLandress et al. (2015) focus on global mean behavior, whereas we examine detailed latitudinal and seasonal structures. Additionally, our calculations include multivariate regression fits, including solar-cycle variations that are especially relevant for characterizing the upper-level SSU channels. Zou and Qian (2016) also derive a merged dataset based on combining SSU and AMSU measurements, utilizing a variational approach to optimally merge the data, and resolving latitude-dependent behavior. Our analyses, based on different datasets and a different merging technique, are a complement to Zou and Qian (2016), and we include some detailed comparisons with the Zou and Qian (2016) results.

We describe the datasets and merging procedure in section 2 and then examine temperature variability in the extended record covering 1979–2015. We focus on quantifying spatial and seasonal patterns of trends in the data, together with the behavior of the 11-yr solar cycle and volcanic-induced temperature effects.

2. Data and analyses

a. Satellite temperature data

Our analyses are based on time series of temperatures in the middle and upper stratosphere from SSU, combined and extended using MLS and SABER. We also include parallel analyses of temperatures in the lower stratosphere based on the Microwave Sounding Unit channel 4 (MSU4) merged with AMSU channel 9 to give perspective to the middle-to-upper stratosphere results. MSU4 represents mean layer temperatures over approximately 13–22 km (Fig. 1a); note that this layer is in the stratosphere in the extratropics but combines the upper troposphere and lower stratosphere in the tropics. We obtain monthly mean MSU4 data covering January 1979–December 2015 from Remote Sensing Systems (http://www.remss.com).

The SSU is a nadir-sounding instrument that measures thermal emission from atmospheric CO_2, with data from seven separate instruments on NOAA operational satellites during November 1978–April 2006. We analyze SSU temperatures based on the recalibrated and merged data product described by Zou et al. (2014). Specifically, we analyze data version 2.0 obtained from the NOAA STAR website (http://www.star.nesdis.noaa.gov/smcd/emb/mscat/index.php). SSU consists of three channels with broad-layer measurements spanning approximately 20–40 km for channel 1 (SSU1), approximately 25–50 km for channel 2 (SSU2), and approximately 30–55 km for channel 3 (SSU3), as illustrated in Fig. 1a. These data are derived using measurements from the separate operational SSU instruments, with the combined record taking account of individual instrument calibration, SSU cell pressure changes, satellite orbit drifts, changes in

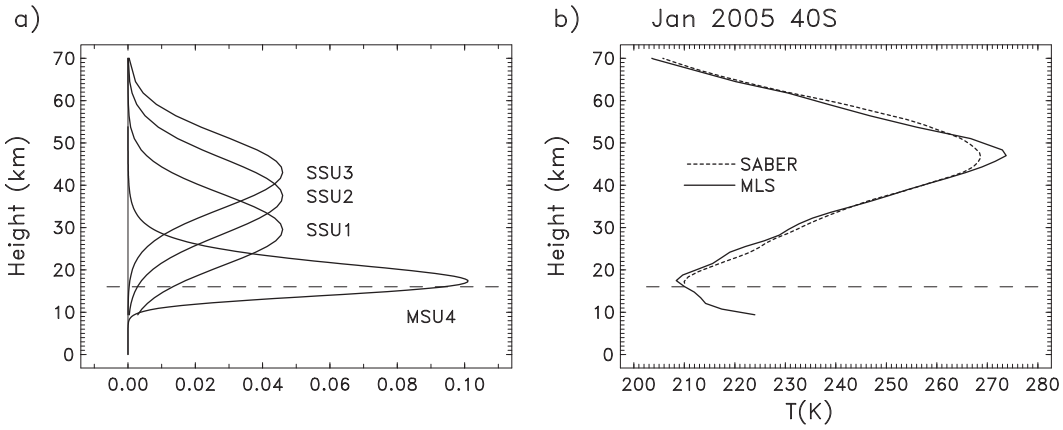

FIG. 1. (a) Weighting functions for SSU-channel and MSU4 satellite measurements analyzed in this study. The SSU-channel weights are the Gaussian-fit structures discussed in the text. (b) Vertical profile of January 2005 zonal-mean temperature at 40°S from MLS and SABER data. The dashed line indicates the lower limit of the SABER data at 16 km.

atmospheric CO_2, and viewing angle differences (Zou et al. 2014). Diurnal sampling variations are adjusted to 1200 local solar time for the merged dataset. We analyze monthly mean SSU data covering January 1979–April 2006. Comparisons with the independent Met Office version 2 analysis of SSU data (Nash and Saunders 2015) show net global mean temperature differences over 1979–2006 of up to approximately 0.5 K for the separate channels (Seidel et al. 2016), but these will produce relatively small differences in trends calculated over 1979–2015. Note that the Met Office version 2 SSU data are available only as 6-month-average global means, so detailed analysis of latitudinal and seasonal variability based on these data is not possible at present.

We extend the SSU temperature record by combining with *Aura* MLS and SABER data. MLS makes measurements of microwave emissions of O_2 from the atmospheric limb, deriving temperatures over altitudes from approximately 10 to 90 km (pressure levels of 261–0.001 hPa), with vertical resolution of approximately 4–7 km over 20–50 km (Schwartz et al. 2008). *Aura* is in a sun-synchronous orbit, with a local equator crossing time of 1345 (0145) on the ascending (descending) node; there has been minimal orbital drift throughout 2004–15, so temperature changes associated with changing local measurement times are small. We utilize MLS retrieval version 4.2 (obtained from https://mls.jpl.nasa.gov/products/temp_product.php). MLS data provide near-global coverage (86°N–86°S) on a daily basis, and we construct and analyze monthly mean data spanning September 2004–December 2015. A short period of missing observations during 27 March–18 April 2011 was filled by linear interpolation prior to forming the monthly means.

The SABER instrument on the *Thermosphere, Ionosphere, Mesosphere Energetics and Dynamics* (*TIMED*) satellite makes measurements of infrared CO_2 emissions from the atmospheric limb. Temperatures are retrieved over altitudes from approximately 16 to 100 km, with a vertical resolution of 2 km (Mertens et al. 2001; Remsberg et al. 2008). Here we use the retrieval version V2.0, which is available online (http://saber.gats-inc.com). SABER temperature profiles are available at two local times each day, with measurements from 53° latitude in one hemisphere to 83° latitude in the other hemisphere. The local times of the measurements shift gradually from one day to the next as the *TIMED* orbit precesses, and this sampling pattern flips approximately every 65 days. Hence, continuous coverage is available over 53°N–53°S and limited for higher latitudes. Furthermore, because it takes about 65 days to cover the full range of local times, only about half of the range will be sampled during any given month, and this can introduce biases in monthly mean values of temperature due to sampling of tides. The different altitude coverage and resolution, as well as tidal sampling, may contribute to the somewhat larger differences with SSU data as compared to MLS, as shown below. We construct and analyze monthly means from the SABER data covering the period February 2002–December 2015. For comparison, Fig. 1b shows the vertical profile of temperature at 40°S for January 2005 based on SABER and MLS data, illustrating small profile differences that contribute to the vertically integrated results shown below.

b. *Merging SSU, MLS, and SABER data*

Our objective is to merge the SSU data (January 1979–April 2006) with equivalent vertically weighted

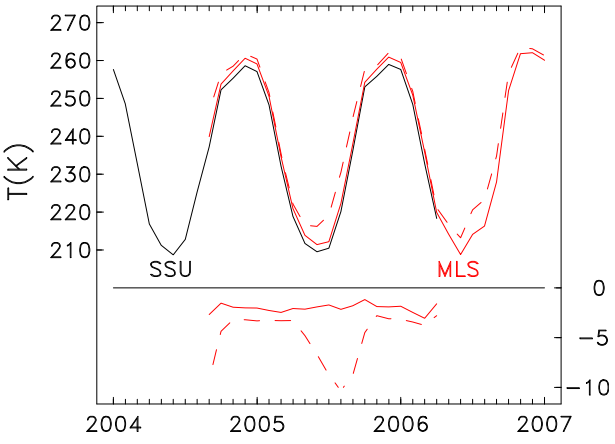

FIG. 2. Curves at top show time series of temperature for SSU2 at 80°S for SSU (black) and vertically integrated MLS (red) data. The curves at bottom are the respective differences (K) for the overlap period during 2004–06. The dashed red lines are based on weighting functions derived from CRTM calculations, and the solid red lines are based on the Gaussian-shaped weighting function (shown in Fig. 3a).

temperatures from MLS (September 2004–December 2015) and SABER (February 2002–December 2015). This will result in two separate datasets spanning 1979–2015. We first construct vertically weighted SSU-equivalent temperatures from the MLS and SABER data by vertically integrating the profile temperatures (e.g., Fig. 1b) using the SSU weighting functions (WFs). Our original calculations utilized latitude- and month-dependent WFs obtained from the NOAA STAR website; these are derived from the SSU Community Radiative Transfer Model (CRTM) described in Chen et al. (2011) and utilized in Wang et al. (2012) and Zou et al. (2014). However, detailed comparisons of the resulting synthesized SSU data with actual SSU measurements showed some substantial seasonally varying biases at polar latitudes, where the stratosphere undergoes a large seasonal cycle. This behavior is shown for SSU channel 2 at 80°S in Fig. 2; the large annual cycle (>50 K) is systematically underestimated by MLS integrated with the CRTM WFs, and such seasonally varying biases will corrupt long-term variability in a merged dataset. Note that any constant, time-mean biases between the datasets can be simply corrected in merged data using the overlap period, but seasonally varying differences need to be minimized. We also tried directly simulating SSU temperatures using the SSU CRTM with MLS temperatures as input and found nearly identical behavior as in Fig. 2. We note that this is mainly a problem in polar regions (where large seasonal variations occur); the standard WF or CRTM calculations work well in low-to-middle latitudes where the seasonal variations are much smaller.

We devised a set of alternative, empirical weighting functions that improve the overall seasonally varying fits to SSU data. These are based on simple Gaussian-shaped weighting functions of the following form:

$$\mathrm{WF}(z) = A_o \exp - [(z - z_o)/D]^2,$$

with z_o and D chosen to minimize the seasonal biases between the synthesized and actual SSU data [the constant A_o is a normalization factor chosen so that the vertical integral of $\mathrm{WF}(z) = 1.0$, and numerically $A_o = (D\sqrt{\pi})^{-1}$]. An example of the resulting Gaussian SSU2 weighting function at 80°S is shown in Fig. 3a, compared with the corresponding SSU2 WFs derived from the SSU CRTM (which vary seasonally; Fig. 3a shows results for January and July at 80°S). The Gaussian-fit WF is chosen based on minimizing the rms difference between SSU and weighted MLS data during the overlap September 2004–April 2006 (after removing the time-mean biases). Variations in rms temperature differences as a function of z_o and D for SSU2 at 80°S (Fig. 2) are shown in Fig. 3b, showing a minimum for z_o of approximately 37.5 km and for D of approximately 12.5 km. The resulting Gaussian WF (Fig. 3a) has similar overall shape and peak maximum as the CRTM results, with slightly enhanced weights for altitudes below the maximum (this is typical for all latitudes). The resulting variations in synthesized SSU2 temperatures at 80°S are shown in Fig. 2, showing a much improved fit to the seasonal cycle compared to the CRTM WFs. We performed this analysis for each latitude and find that the best-fit results for z_o and D depend only weakly on latitude or season, and so for simplicity we choose constant global-average values for z_o and D for each SSU channel (listed in Table 1). These WFs provide an improved empirical fit of the seasonal cycle for polar regions compared to the CRTM results (with little difference over low-to-middle latitudes). The reasons for these differences with CRTM are not understood at present but could possibly be related to altitude biases in the MLS retrievals; Schwartz et al. (2008) report a positive height bias for the MLS temperature retrievals of 150 m at 100 hPa, increasing with altitude, and this could explain part of the WF differences discussed above.

We obtain slightly different results for optimum z_o and D for SABER data, likely because of different effective vertical resolutions between MLS and SABER and the fact that MLS extends farther downward (10 km) than SABER (16 km) (Fig. 1b). The differences are larger for SSU channel 1, which includes small but significant contributions from lower altitudes. Using the optimized Gaussian WFs for SABER results in slightly larger rms differences with SSU as compared to the

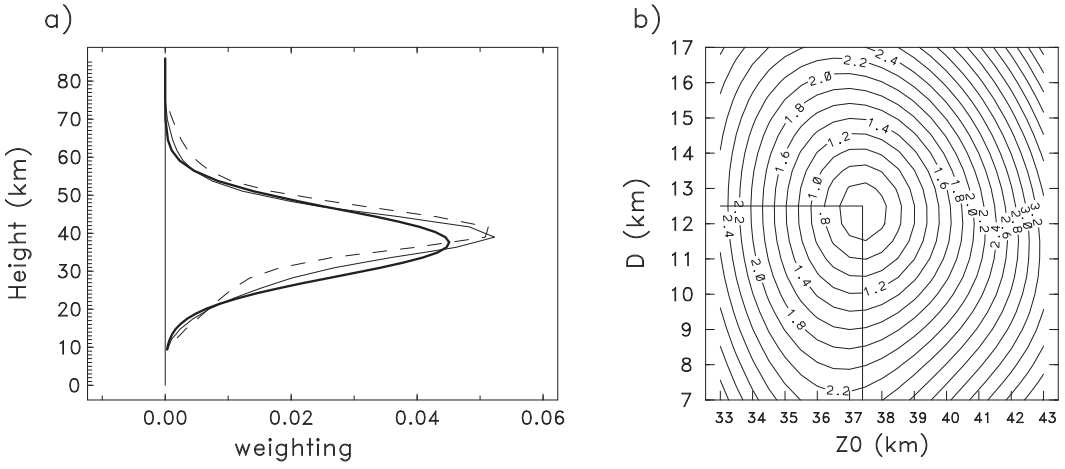

FIG. 3. (a) Weighting functions for SSU2 at 80°S. Thin lines show results from CRTM calculations for January (solid) and July (dashed), and thick line shows the Gaussian-shaped fit discussed in the text. (b) Contour plot of the rms difference (K) between SSU2 at 80°S (time series in Fig. 2) and vertically integrated MLS data using the Gaussian-fit weighting function, as a function of the parameters z_o and D. The minimum rms value corresponds to the best-fit choices for z_o and D (noted by lines).

synthesized MLS results, including small seasonally dependent differences. However, we utilize SABER mainly to compare annual mean results with MLS over 53°N–53°S and so are less concerned with small seasonally varying biases in SSU-synthesized SABER data.

The above calculations produce monthly temperatures as a function of latitude for each SSU channel, based on vertically integrated MLS and SABER data. We then deseasonalize the respective time series by subtracting a mean seasonal cycle derived from the merged SSU + MLS data over 1979–2015 (after removing time-mean biases based on the SSU–MLS overlap period). These provide deseasonalized anomalies for each dataset. We then normalize each deseasonalized dataset (SSU and SSU-equivalent MLS and SABER data) to each have zero time mean for the one-year direct overlap period January–December 2005; temperature anomalies for the rest of this work are simply defined compared to this period.

The deseasonalized anomalies for one channel (SSU2) at several latitudes (0°, 50°, and 80°S) are shown in Fig. 4 for each of the SSU, MLS, and SABER datasets. SSU and SABER directly overlap during February 2002–April 2006, during which period the respective anomalies in Fig. 4 track each other closely (with small rms differences of ~0.5 K). SSU overlaps MLS during September 2004–April 2006, with nearly identical variations in Fig. 4 (and rms differences of ~0.3 K). The MLS and SABER data also track each other closely in Fig. 4 for the longer overlap period 2004–15; while there are small seasonally varying differences between these

TABLE 1. Coefficients for the Gaussian SSU weighting functions.

SSU channel	z_o (km)	D (km)
SSU3	43.1	12.3
SSU2	37.4	12.8
SSU1	29.5	12.1

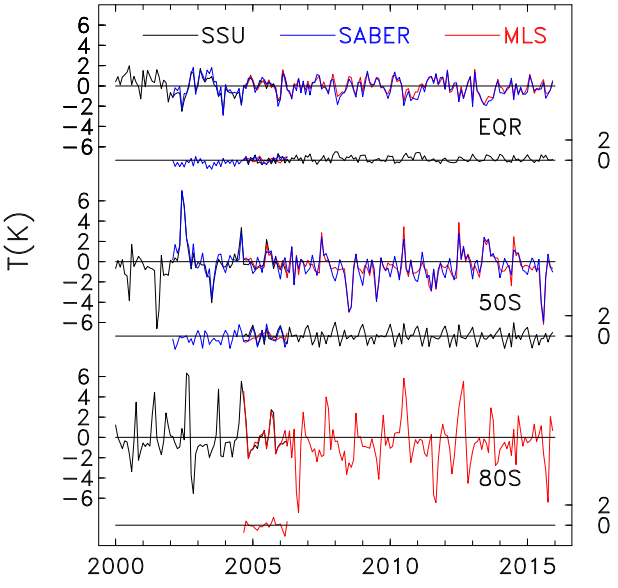

FIG. 4. Time series of deseasonalized temperature anomalies for SSU2 at the equator, 50°S, and 80°S from top to bottom for SSU, SABER, and MLS data. The lower set of curves for each latitude show the respective differences (K) during the direct overlap time periods [SSU − SABER (blue), SSU − MLS (red), and MLS − SABER (black)].

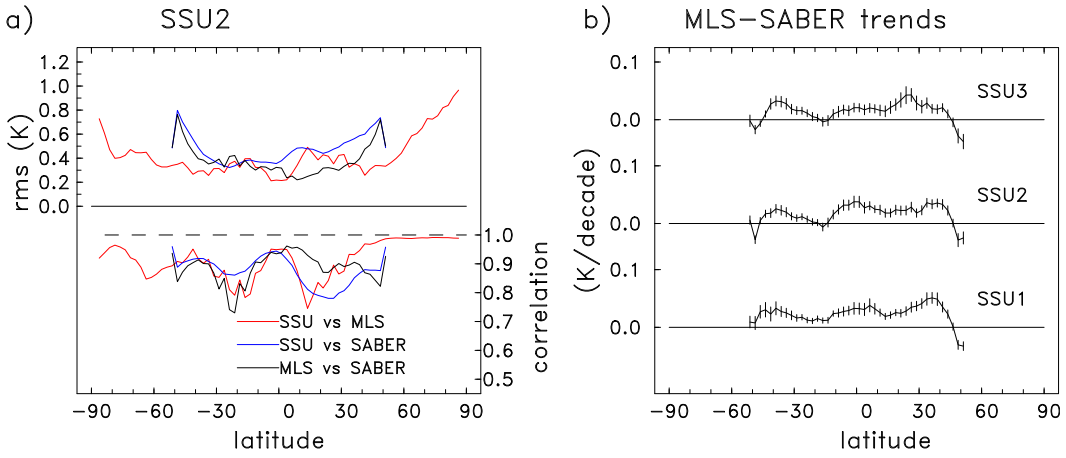

FIG. 5. (a) Statistics of the deseasonalized temperature anomaly correlations and rms differences as a function of latitude for SSU2 (as shown in Fig. 4). Lower curves show the anomaly correlations, and upper curves show the rms values of the respective differences, calculated for the respective overlap periods. (b) The linear trends in the time series of differences between vertically integrated MLS and SABER data, for the overlap period 2005–15. Error bars show the 2σ statistical uncertainty.

data, there are no long-term drifts evident over this period.

Comparisons as in Fig. 4 for each SSU channel and each latitude show excellent agreement among the datasets, and summary statistics of anomaly correlations and rms differences as a function of latitude for SSU2 are shown in Fig. 5a. Anomaly correlations are extremely high (>0.8), and rms differences for the overlap periods are typically 0.2–0.5 K (larger in polar regions). There are slightly larger rms differences involving SABER data because of small systematic seasonal differences as seen at 50°S in Fig. 4. Overall similar results are found for SSU1 and SSU3 (not shown). Linear trends in the MLS–SABER differences for the overlap 2004–15 are shown in Fig. 5b for each of the SSU channels. Trend results for each channel are very small (<0.05 K decade^{-1}), demonstrating almost no systematic drifts between the MLS and SABER data.

Overall we find excellent agreement for temperature anomalies in the SSU, MLS, and SABER datasets for the respective overlap periods. Based on this excellent agreement, we construct merged data by simply combining the SSU with MLS (taking averages of both instruments during the overlap period) and likewise (separately) combining SSU with SABER. Because the SSU + SABER data are limited to 53°N–53°S (because of SABER sampling), we focus most of our analyses on the combined SSU + MLS data (and include some brief comparisons with SSU + SABER).

c. *Comparisons with SSU + AMSU results*

Zou and Qian (2016) have recently developed a merged dataset combining SSU + AMSU measurements, and it is useful to briefly compare those data with our SSU + MLS and SSU + SABER results. We obtained the merged SSU + AMSU data from the STAR website (http://www.star.nesdis.noaa.gov/smcd/emb/mscat/index.php). Note that the merging of SSU with AMSU begins in 2001, with SABER in 2002, and with MLS in 2004, and hence the datasets are identical before 2001.

Time series of differences between SSU + MLS and SSU + AMSU data for SSU3 over latitudes 80°N–80°S are shown in Fig. 6a. Differences are very small prior to late 2004 (beginning of MLS data), while larger seasonally varying differences occur throughout the rest of the record (largest at high latitudes). Because the Zou and Qian (2016) merged SSU + AMSU data partly depend on the CRTM weighting functions for SSU, these seasonally varying differences in Fig. 6a possibly reflect the same issues in fitting the seasonal cycle as discussed above in relation to Figs. 2 and 3. Similar but smaller-magnitude differences are found for SSU1 and SSU2 (not shown). rms differences between the MLS and AMSU datasets during 2005–15 (Fig. 6b) show relatively small values of 0.2–0.6 (and larger for polar regions), increasing from SSU1 to SSU3. Linear trends between the datasets for the period 2005–15 are shown in Fig. 7, including MLS–AMSU and SABER–AMSU results. Trends are very small for SSU1 and increase slightly for SSU2 and SSU3 (reaching 0.4 K decade^{-1} in low latitudes for SSU3), although none of the trends is statistically significant in this short record. The different trends between AMSU, MLS, and SABER over 2005–15 result in relatively small differences for longer-term calculations with the merged SSU datasets, as shown below.

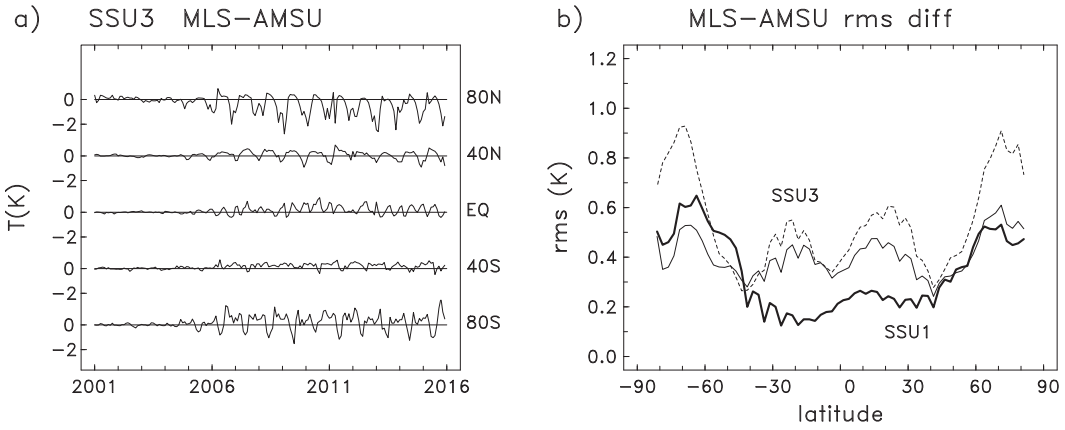

FIG. 6. (a) Time series of differences between SSU + MLS and SSU + AMSU data for SSU3 at several latitudes over 80°N–80°S. (b) RMS differences between SSU + MLS and SSU + AMSU data calculated over 2005–15 for each of the SSU channels.

Overall our comparisons show very good agreement with the SSU + AMSU results, with slightly larger rms differences and trends for SSU3 compared to SSU1 and SSU2. This is consistent with the larger uncertainty in SSU3 derived from merged SSU + AMSU data, as discussed in Zou and Qian (2016).

d. Regression analysis

To identify and isolate particular climate signals in the temperature data, we perform a standard multivariate linear regression analysis (e.g., Randel et al. 2009). The regressions include terms to account for linear trends, 11-yr solar cycle [using the solar radio flux at 10.7 cm (F10.7) as a proxy], two orthogonal time series to model the quasi-biennial oscillation (QBO) (Wallace et al. 1993), and an El Niño–Southern Oscillation (ENSO) term [based on the multivariate ENSO index (MEI) from the NOAA/ESRL Physical Sciences Division (former Climate Diagnostics Center; http://www.esrl.noaa.gov/psd/enso/mei/)]. Our regression analyses include annual and semiannual variations in the fits for each term. We analyze linear trends over the entire 1979–2015 record to quantify long-term changes, and we also include analyses of separate linear fits over the two halves of the data record (1979–97 and 1998–2015) because of anticipated responses to changes in stratospheric ozone trends (e.g., Stolarski et al. 2010). While we include QBO and ENSO terms in the regression fits, our main focus is on decadal-scale variations and trends. We do not include a proxy for volcanic aerosols in our regressions but rather exclude two years of data after the large volcanic eruptions of El Chichón (April 1982) and Mt. Pinatubo (June 1991) in the regression fits (two years is the approximate time scale for the largest volcanic temperature anomalies; e.g., Free and Lanzante 2009). In this case the temperature effects of the volcanoes appear in the residuals to the regression fits, as shown below. Uncertainty estimates for the statistical fits are calculated using a bootstrap resampling technique (Efron and Tibshirani 1993), which includes the effects of serial autocorrelation.

Monthly variations of the long-term linear trends are calculated somewhat differently. We simply calculate regression fits for each individual month (including the solar, QBO, and ENSO terms) and contour the results for all months in a combined plot. This allows more accurate definition of month-to-month variations, as compared to fitting annual and semiannual harmonics.

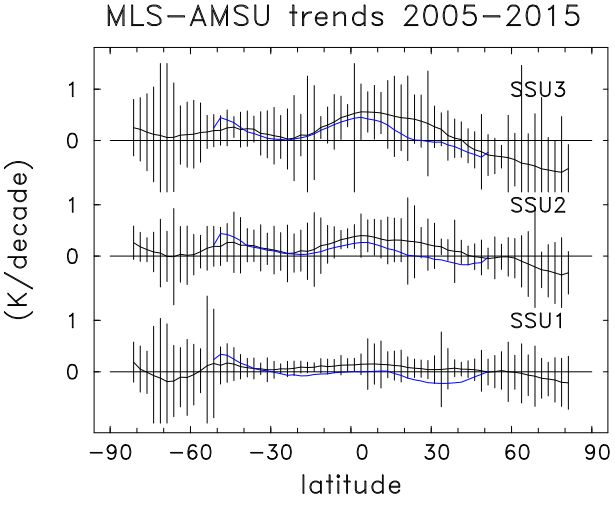

FIG. 7. Black lines show linear trends of the differences between SSU + MLS and SSU + AMSU data, calculated over 2005–15. Error bars show the 2σ statistical trend uncertainties for this short record. Blue lines show the corresponding trends for differences between SSU + SABER and SSU + AMSU data.

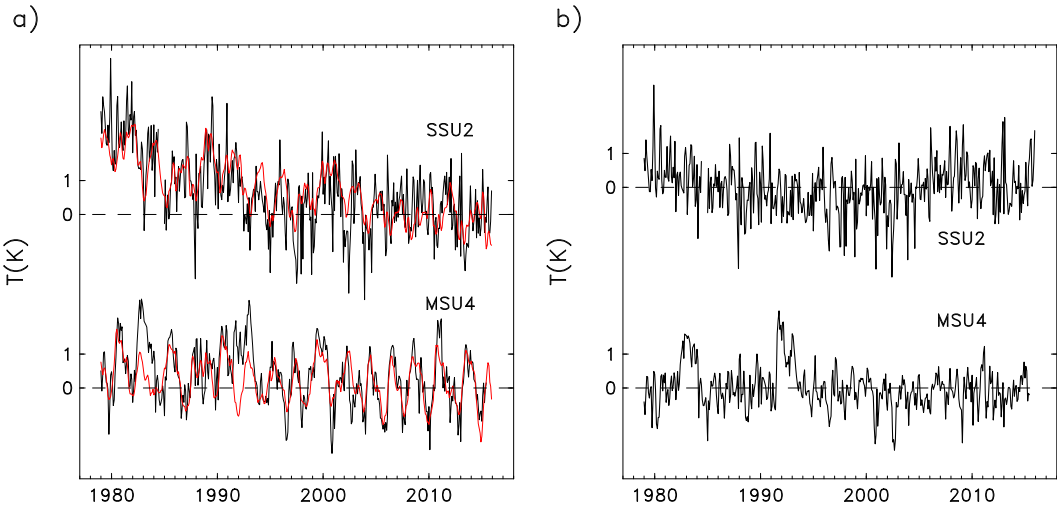

FIG. 8. (a) Time series of deseasonalized temperature anomalies at the equator for MSU4 and SSU2 data. The red lines show the multiple linear regression fit of these time series. (b) Time series of differences between the temperature anomalies and regression fits in (a) for each satellite channel.

3. Results

a. Time series, regression fits, and residuals

Time series of the deseasonalized zonal mean temperature anomalies for MSU4 and SSU2 (from SSU + MLS data) at one particular latitude (the equator) are shown in Fig. 8a, together with the regression fit of the anomalies (red lines). The residuals of the fits are shown in Fig. 8b. The corresponding time series for SSU1 and SSU3 are similar to SSU2 (not shown). There is a strong QBO variation in the MSU4 time series in Fig. 8a that is accurately captured in the regression, and warming linked to the volcanic eruptions of El Chichón and Mt. Pinatubo is clearly evident in the residuals for MSU4. SSU2 in Fig. 8a shows substantial variability superimposed on long-term cooling, and evidence of solar cycle and QBO variations are also seen in the data (although the QBO is not as evident in the SSU time series as compared to MSU4 because the broad SSU weighting functions smear the relatively narrow QBO signal). The SSU2 residuals at the equator in Fig. 8b show less evidence of volcanic influence than MSU4 and show more month-to-month variability than the MSU4 data. The residuals for SSU2 also show persistent negative anomalies during about 1988–2003, and this is the result of fitting a constant linear trend over the entire 1979–2015 record; as shown below, more accurate fits are provided by calculating separate linear trends over the first and second halves of the data record.

The regression model incorporating linear trend, solar, QBO, and ENSO terms captures a large fraction of the variance in the deseasonalized data over latitudes of around 45°N–45°S, as shown in Fig. 9. Relatively larger fractions of variance are explained for the SSU channels over this domain as compared to MSU4, attributable mainly to linear trend and solar components (as shown below). Results in Fig. 9 for MSU4 show maxima at the equator and near 40°N and 40°S, mainly attributable to the tropical and extratropical lobes of the QBO and ENSO signals (e.g., Seidel et al. 2016). In general the regressions do not explain significant fractions of variance in polar regions, where there is large natural month-to-month variability during winter and spring.

Global average anomalies for the four satellite channels are shown in Fig. 10a, and globally averaged residuals from

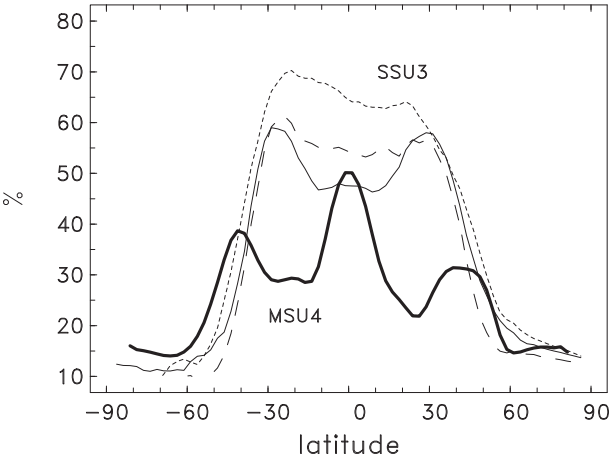

FIG. 9. Percent variance explained by the multivariate linear regression model for each satellite channel as a function of latitude. The thin solid line is for SSU1, and long-dashed line is for SSU2.

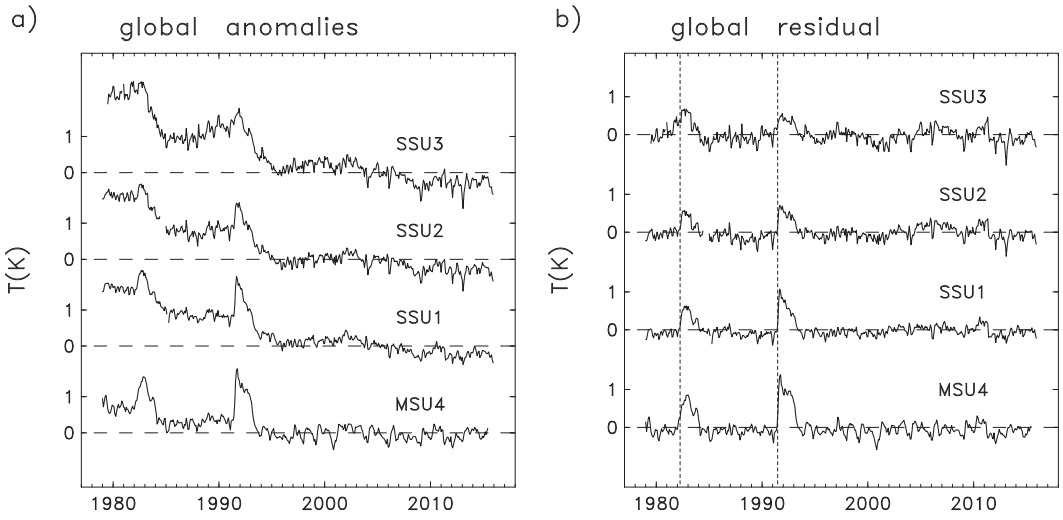

FIG. 10. (a) Time series of global average temperature anomalies for MSU4 and SSU + MLS data. (b) Global average differences between temperature anomalies and regression fits for each satellite channel; the regression includes separate linear trends over 1979–97 and 1998–2015. The dashed vertical lines highlight the volcanic eruptions of El Chichón and Mt. Pinatubo.

the regression fits are shown in Fig. 10b (here the regression model includes separate linear fits over 1979–97 and 1998–2015, as discussed in more detail below). Global anomalies show decadal-scale cooling in each time series, with stronger cooling in the SSU channels compared to MSU4. Volcanic warming signals are evident in the global residuals, clearly extending into the middle and upper stratosphere.

b. *Volcanic signals*

The global average residuals (Fig. 10b) show the influence of volcanic eruptions on stratospheric temperatures, and the spatial structure of the volcanic signals can be examined using the residuals. Figure 11 shows the latitudinal structure of temperature anomalies following El Chichón and Mt. Pinatubo, calculated as residuals averaged over one year following each eruption (April 1982 and June 1991, respectively) minus the average of the three years preceding each eruption. In both cases a strong tropically centered warming signal (~1.0–1.5 K) is seen in the lower-stratosphere MSU4 channel, with smaller tropical warming in SSU1 and near-zero tropical signals in SSU2 and SSU3. Conversely, there are warm anomalies in each of the SSU channels at high latitudes in both hemispheres, with smaller effects in MSU4. Thus, while the globally averaged residual time series (Fig. 10b) show in-phase volcanic temperature effects spanning the lower to upper stratosphere, the

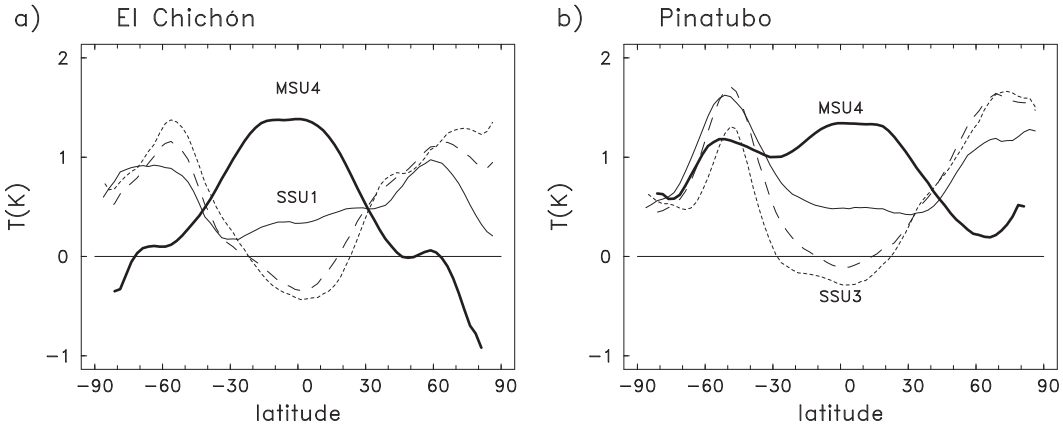

FIG. 11. Latitude profiles of temperature anomalies for one year following the eruption of (a) El Chichón and (b) Mt. Pinatubo. Anomalies are calculated as differences between the full temperature anomalies and multivariate regression fits (excluding these volcanic periods).

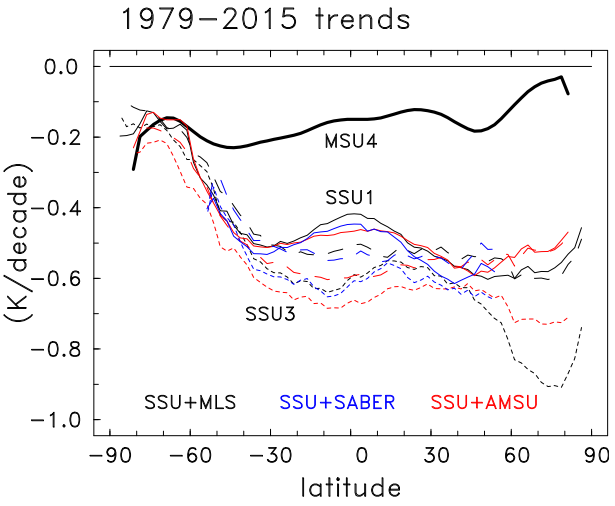

FIG. 12. Latitude profile of linear trends over 1979–2015 for zonal average MSU4 and SSU + MLS data (for each SSU channel; black lines). Blue lines show the corresponding trends derived from SSU + SABER data, and red lines are from SSU + AMSU. Statistical uncertainties at 2σ for these trends are near 0.1 over low-to-middle latitudes and above 0.3 for polar latitudes (because of much larger natural variability over the poles).

latitudinal structure is very different between the lower stratosphere (tropical warming) and the middle-to-upper stratosphere (high-latitude warming and small tropical signals). Overall very similar patterns are seen for the El Chichón and Mt. Pinatubo events in Fig. 11, suggesting a robust signature for these large tropical volcanic eruptions (as discussed further below).

c. *Linear trends over 1979–2015*

We evaluate linear trends calculated over the entire record 1979–2015 to highlight the latitudinal and seasonal behavior of stratospheric temperature changes over almost four decades. The latitudinal structure of annual average zonal mean trends from MSU4 and the different merged SSU datasets are shown in Fig. 12; trends and statistical uncertainties for global means are included in Table 2. MSU4 shows long-term cooling from approximately −0.15 to $-0.20\,\mathrm{K\,decade^{-1}}$ with relatively little variation in latitude (and near-zero trends in the Arctic). The three separate merged SSU datasets show reasonably similar results in terms of magnitude and latitudinal structure. The SSU data show cooling from approximately −0.50 to $-0.60\,\mathrm{K\,decade^{-1}}$ over much of the globe north of 30°S, while cooling significantly decreases at higher SH latitudes, producing a marked asymmetry in cooling patterns over the globe (note that this behavior is seen in each of the merged SSU datasets). In the low latitudes, cooling trends increase slightly from SSU1 to SSU3 (i.e., the trends increase from the middle to the upper stratosphere).

TABLE 2. Linear trends ($\mathrm{K\,decade^{-1}}$) and 2σ uncertainties in global average temperatures in parentheses. SSU results are from the merged SSU + MLS data.

Satellite channel	1979–2015	1979–97	1998–2015
SSU3	−0.58 (0.07)	−0.89 (0.08)	−0.28 (0.07)
SSU2	−0.50 (0.08)	−0.86 (0.06)	−0.19 (0.06)
SSU1	−0.48 (0.06)	−0.76 (0.05)	−0.23 (0.05)
MSU4	−0.17 (0.06)	−0.34 (0.03)	0.01 (0.03)

Trend results based on the SSU + SABER data are nearly identical to the SSU + MLS results in Fig. 12, enhancing confidence in both estimates (and consistent with the very small trends in MLS–SABER differences in Fig. 5b). Trends from SSU + AMSU are slightly larger in the tropics for SSU2 and SSU3 but well within statistical uncertainties. There are larger trend differences in the Arctic upper stratosphere for SSU3, but these have large statistical uncertainties (2σ values of $\sim 0.5\,\mathrm{K\,decade^{-1}}$). The consistent results in Fig. 12 among the very different data sources give confidence to the overall SSU results.

The monthly variation of trends over 1979–2015 as a function of latitude for each of the satellite channels are shown in Fig. 13, based on trend calculations for each individual month (as described in section 2). In these plots colors denote trends that are statistically significant at the 95% level. MSU4 (Fig. 13a) shows relatively small cooling trends ($<-0.2\,\mathrm{K\,decade^{-1}}$) over most of the globe, with regions of statistical significance in the midlatitudes during summer–autumn (~30°–60°S during December–May and ~30°–60°N during August–October) and also in Arctic polar latitudes during summer (a region with small background variability). There are relatively larger trends in the polar regions of both hemispheres during winter–spring (regions of large natural variability), but none of these trends is statistically significant. It is interesting that while shorter records of MSU4 highlighted significant cooling during Antarctic spring, associated with development of the ozone hole [e.g., trends over 1979–97 in Randel and Wu (1999)], such trends are not significant in the longer record of MSU4 extending to 2015.

Latitude–month trends over 1979–2015 for the three SSU channels based on SSU + MLS (Figs. 13b–d) show similar overall patterns for the three channels, with statistically significant cooling ($\sim -0.6\,\mathrm{K\,decade^{-1}}$) over approximately 40°N–40°S. There are latitude- and season-dependent variations in these trends, but the statistical uncertainty for individual months is relatively

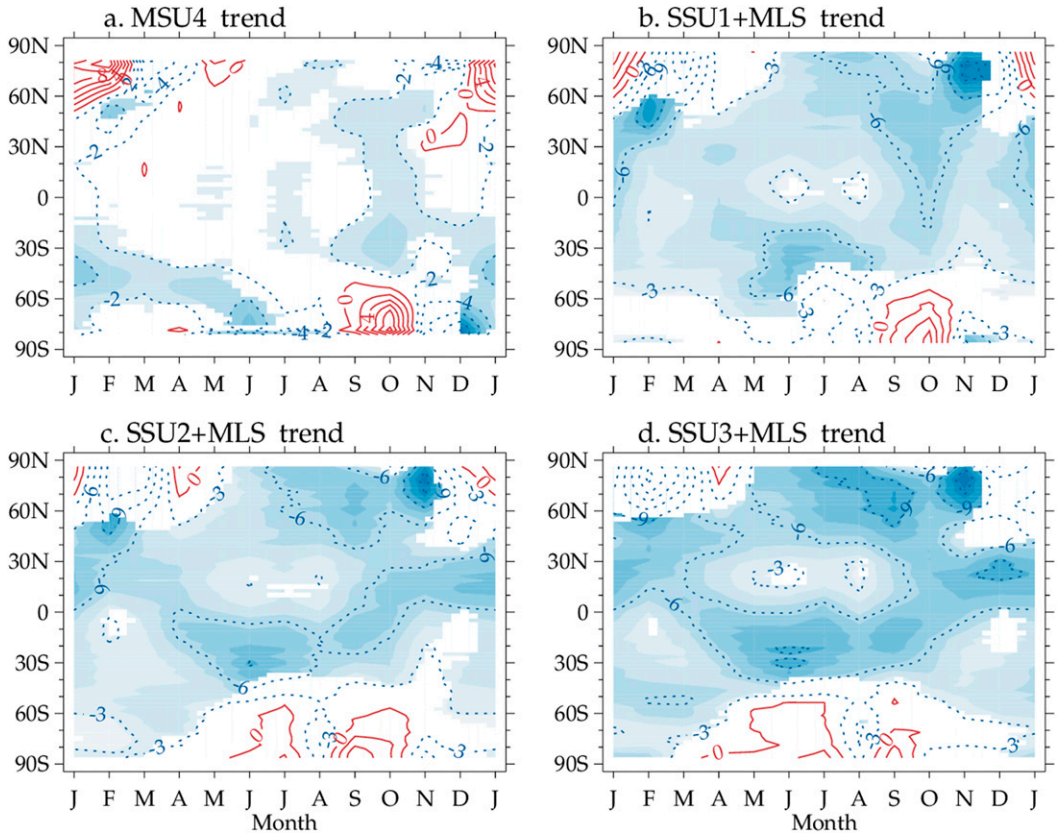

FIG. 13. Latitude–month variation of linear trends in temperature from (a) MSU4 and merged (b)–(d) SSU + MLS data calculated over 1979–2015. Contour interval is 0.2 K decade^{-1} in (a) and 0.3 K decade^{-1} in (b)–(d) for each of the SSU channels. The blue shading denotes trends that are significant at the 95% level.

high (~0.3 K decade^{-1}), so interpretation should focus on broad-scale features. Slightly stronger cooling trends are seen in the upper stratosphere over approximately 0°–40°S during SH winter (~May–September) and approximately 0°–40°N for NH winter (November–February), with weaker trends in the respective summer low latitudes during these months. Strong and highly significant cooling occurs over the Arctic during summer (June–September); weaker and marginally significant cooling also occurs over the Antarctic in summer (DJF) for the upper-level channels SSU2 and SSU3. Polar trends in the SSU + MLS data during winter–spring in both hemispheres are highly variable and statistically insignificant because of large natural year-to-year variability.

To illustrate the behavior of polar temperatures, Fig. 14 shows time series of seasonal average polar cap anomalies for the Arctic and Antarctic, including results for the lower stratosphere (MSU4) and upper stratosphere (SSU3). These data highlight the well-known behavior of low variability during summer and autumn and enhanced variability during winter–spring. In the Arctic winter (DJF), variability increases from the lower to the upper stratosphere, while in the Antarctic spring (SON) the variance maximizes in the lower stratosphere. As quantified in Fig. 13, there are no statistically significant long-term temperature trends in the winter–spring seasons in either hemisphere. The Arctic summer (JJA) upper stratosphere shows remarkably clear cooling trends superimposed on a background of very small year-to-year variability.

d. Solar cycle

While the solar cycle is not the main focus of this work, the extended record of SSU, MLS, and SABER data provides an opportunity to evaluate this variability for a little over three complete solar cycles. The extended record also helps separate the solar influence from volcanic effects because of the approximate overlap of solar maximum conditions with El Chichón and Mt. Pinatubo (e.g., Lee and Smith 2003) (although these volcanic periods are omitted from our regression analysis). Latitudinal structure of the temperature solar cycle from the MSU4 and SSU + MLS data are shown in Fig. 15, showing an increase in amplitude from the lower to the upper stratosphere, with a magnitude of about

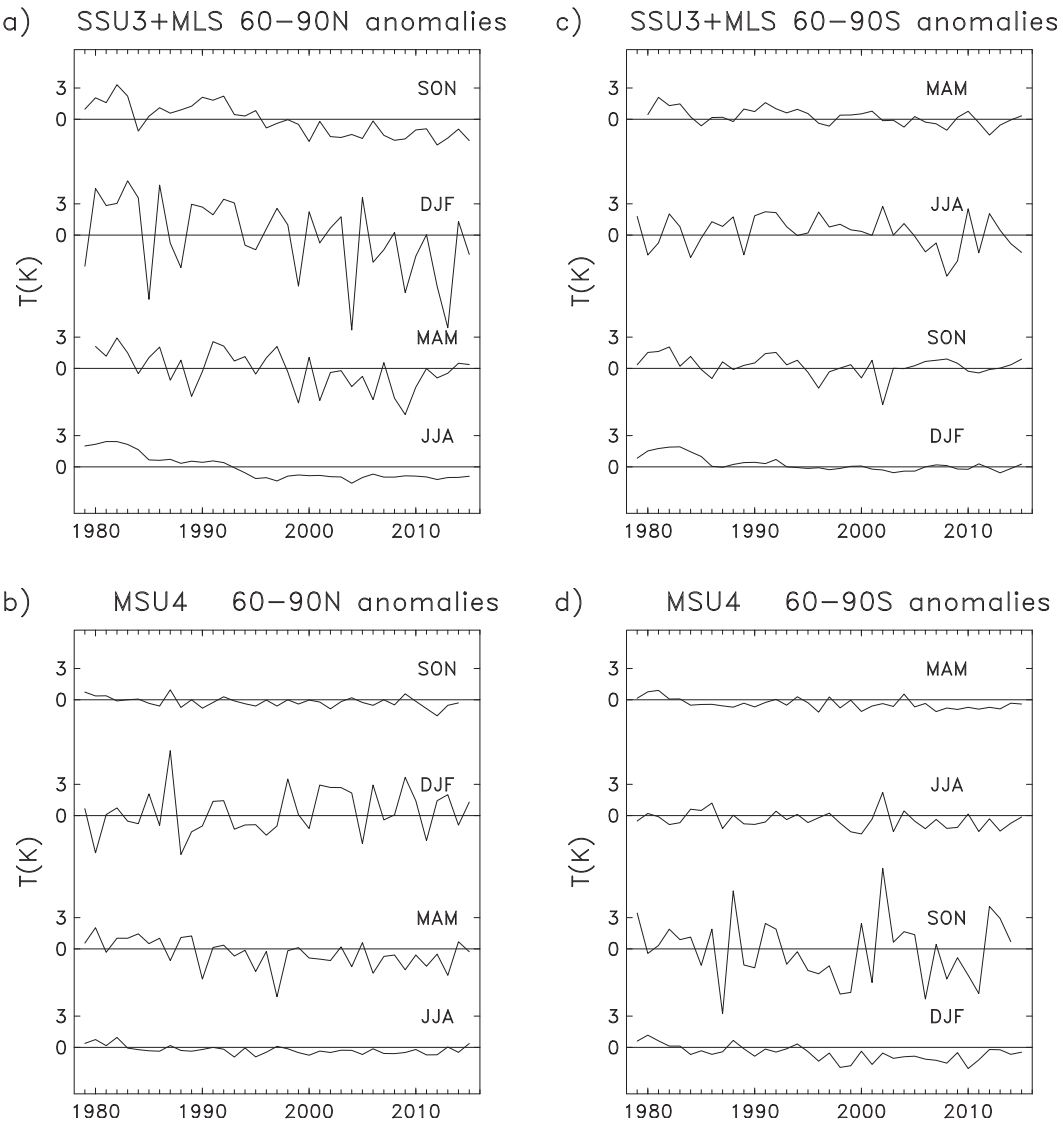

FIG. 14. Time series of polar cap temperature anomalies for the (a),(b) Arctic and (c),(d) Antarctic, for measurements covering the (bottom) lower stratosphere (MSU4) and (top) upper stratosphere (SSU3 + MLS). Anomalies in each panel are segregated according to season.

0.7 K (100 units F10.7)$^{-1}$ in the upper stratosphere. The solar signal is centered in the tropics and is statistically significant over approximately 40°N–40°S. Relative minima occur over approximately 40°–50°N and 40°–50°S, and the relatively large solar cycle projections at high latitudes are not significant in these results. Very similar results are derived from the SSU + SABER and SSU + AMSU datasets (not shown).

e. Differences in trends before and after 1997

Model calculations have shown that stratospheric temperature trends are mainly attributable to increases in atmospheric CO_2 (leading to cooling) plus the radiative effects of stratospheric ozone changes (e.g., Shine et al. 2003; Stolarski et al. 2010). Ozone in the upper stratosphere exhibited strong decreases prior to about 1997 and increases after about 1998 (Bourassa et al. 2014; Kyrölä et al. 2013), as a response to changes in stratospheric halogen loading (WMO 2014). The statistical significance of the ozone increases after 1998 depends on the details of the datasets and uncertainty calculations (Harris et al. 2015), although the changes in ozone trends compared to the 1979–97 period are a robust result. Accordingly, we anticipate that there may be changes in stratospheric temperature trends following these observed ozone changes, with stronger cooling

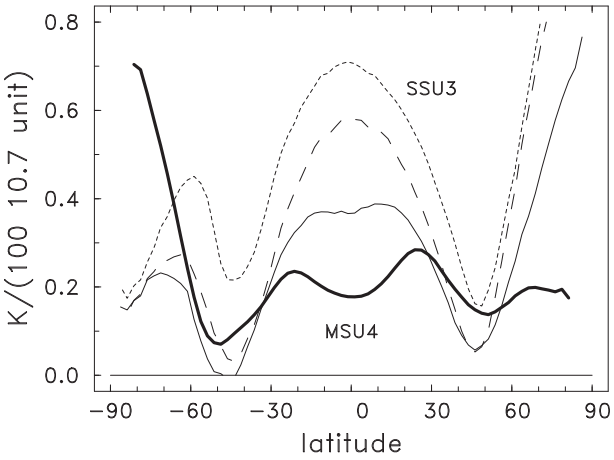

FIG. 15. Latitude profile of solar cycle regression fit over 1979–2015 for each satellite channel. The thin solid line is for SSU1, and long-dashed line is for SSU2. Statistical uncertainties at 2σ for each channel are approximately 0.2–0.3 K (100 units F10.7)$^{-1}$over 50°N–50°S and much higher [above 0.6 K (100 units F10.7)$^{-1}$] over polar latitudes.

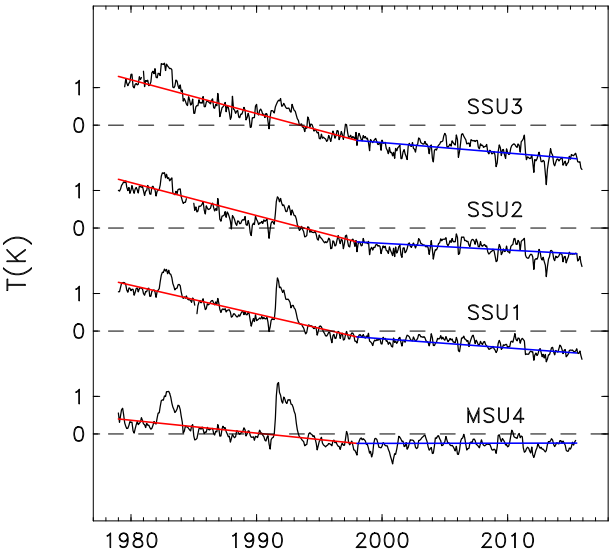

FIG. 16. Global average temperature anomalies for four satellite channels, after removal of the solar cycle, QBO, and ENSO regression fits. The red and blue straight lines show linear trend fits over 1979–97 and 1998–2015, respectively.

trends before about 1997 [as seen in the model calculations of Stolarski et al. (2010)].

Figure 16 shows global average temperature anomalies for the four satellite channels, where we have removed the solar cycle, QBO, and ENSO effects (but not the linear trends over 1979–2015). Figure 16 shows linear fits to the time series for the two separate periods 1979–97 and 1998–2015, showing a change in slope between the two periods for each channel, with stronger cooling for the former time period. The global average trends for these two periods are listed in Table 2, showing that the change in cooling trends is statistically significant for each channel. Similar conclusions have been reached using different time periods and extensions of the SSU datasets by McLandress et al. (2015), Seidel et al. (2016), and Zou and Qian (2016).

The latitudinal structure of the zonal mean temperature trends for the 1979–97 and 1998–2015 periods are shown in Fig. 17, highlighting contrasting behavior between the two periods. During 1979–97 (Fig. 17a), cooling trends in the middle-to-upper stratosphere (SSU channels) are large (from ~ -0.8 to -1.1 K decade^{-1}) over much of the globe ($\sim$30°S–60°N), with small trends over high latitudes. The 1979–97 MSU4 trends show contrasting structure with small trends in the tropics and larger cooling trends at high latitudes of both hemispheres (trends in the Arctic for this period were strongly influenced by a sequence of cold, low-ozone years during the mid-1990s; Randel and Wu 1999). The behavior is very different for 1998–2015 (Fig. 17b), with relatively smaller trends for SSU channels (from ~ -0.2 to -0.4 K decade^{-1}) and no significant trends for MSU4. These strong differences in temperature trends between the two periods are consistent with the influence of changes in stratospheric ozone, as discussed further below.

4. Summary and discussion

SSU provided the longest observational record of mid- and upper-stratospheric temperatures, spanning 1979–2006 (from seven separate operational satellite instruments). We have utilized the new NOAA STAR version of the recalibrated and merged SSU data record (Zou et al. 2014) and extended these measurements through 2015 with equivalent layer-mean temperatures derived from MLS and SABER data to create novel records of stratospheric temperatures spanning 1979–2015. We have utilized a set of empirically derived Gaussian WFs to create SSU equivalent temperatures from MLS and SABER data. These Gaussian WFs provide a much improved fit of the large annual cycle of SSU temperatures at polar latitudes, compared to the WFs derived from SSU CRTM calculations (and do a similarly good job at low-to-middle latitudes). The resulting temperature variations show excellent agreement among SSU, MLS, and SABER data for the available overlap periods (Figs. 4 and 5). There is also good agreement between the MLS and SABER data during 2004–15 with very small time-varying drifts (Fig. 5b). We have combined the SSU with MLS and separately with SABER and find virtually identical

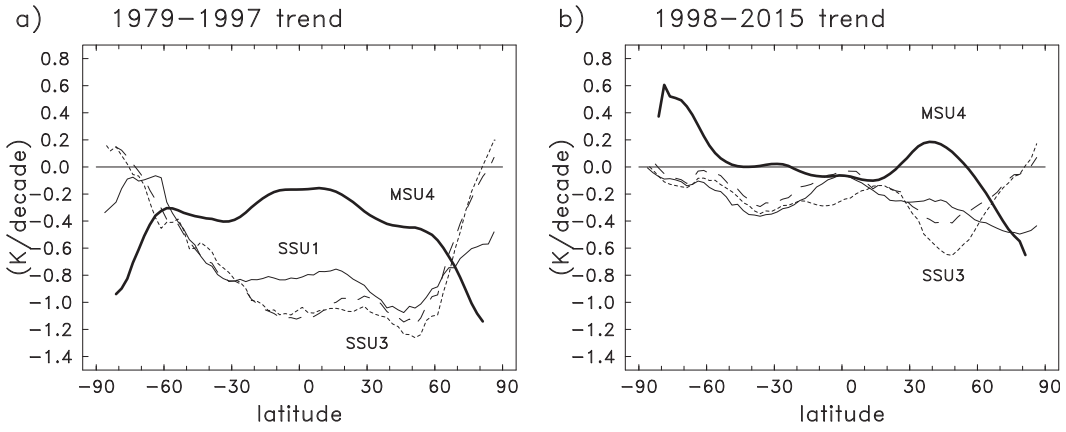

FIG. 17. Latitude profiles of zonal average temperature trends for each satellite channel, derived for time samples over (a) 1979–97 and (b) 1998–2015. For both periods, 2σ statistical uncertainties are of order 0.1–0.2 K decade^{-1} over low-to-middle latitudes and larger (0.3 K decade^{-1} or above) over polar latitudes.

variability between the two datasets (over 53°N–53°S); we have focused most of our analyses on SSU + MLS because of limited sampling of polar regions by SABER.

We have also included comparisons with the merged SSU + AMSU dataset from Zou and Qian (2016) and find small seasonally varying biases and relatively small rms differences with SSU + MLS data, largest for SSU3 (Fig. 6). Trends of differences between AMSU and MLS or SABER data during 2005–15 (Fig. 7) are largest for SSU3 (with maximum near 0.4 K decade^{-1} over low latitudes) but with large statistical uncertainties for the short record. Overall the different merged SSU datasets show good agreement, with slightly larger differences for the upper-level SSU3. The merged datasets produced in this study (both full and deseasonalized datasets) are available via anonymous ftp at ftp://ftp.acom.ucar.edu/user/randel/SSUdata.

Standard multiple regression analysis reveals coherent signatures of linear trends, solar cycle, QBO, and ENSO, which explain large fractions of variance in MSU4 and SSU time series outside of polar regions. While significant QBO signals are seen for all of the satellite channels and likewise for ENSO in MSU4 (but not SSU; see Seidel et al. 2016), our main focus is on the long-term trends and solar signal, for which these data provide novel information. Residuals from the regression fits highlight global-scale warm anomalies linked with the volcanic eruptions of El Chichón (1982) and Mt. Pinatubo (1991). The patterns of stratospheric warming are similar for both eruptions (Fig. 11), showing tropical warming in the lower stratosphere (in MSU4 and much weaker in SSU1) combined with high-latitude warming in each of the SSU channels. Hence, although the global mean anomalies show a clear volcanic influence for all four satellite channels (Fig. 10b), the characteristic latitudinal structure varies strongly with altitude. The lower-stratospheric tropical warming is a well-known volcanic signal (e.g., Free and Lanzante 2009; Fujiwara et al. 2015) and is a direct radiatively forced result due to high aerosol loading (e.g., Robock 2000). The systematic high-latitude warming observed in the middle and upper stratosphere in SSU data is not well understood; note that volcanic aerosols are not observed in high latitudes of the upper stratosphere in satellite observations (Thomason and Peter 2006), which argues against a direct radiative influence. Mitchell et al. (2014) and Fujiwara et al. (2015) have recently derived volcanic temperature signals based on reanalysis datasets and find high-latitude warming in the upper stratosphere for several recent-generation reanalyses, although the statistical significance of the signals varies among datasets and they do not speculate on possible physical mechanisms. One possibility is that these high-latitude, symmetric temperature patterns may be the signature of an intensification of the deep branch of the stratospheric overturning Brewer–Dobson circulation following the volcanic eruptions, although a purely dynamical response would not be expected to lead to a global average temperature change (as seen in Fig. 10b).

The solar signal derived from the extended record of MSU4 and SSU + MLS data (Fig. 15) shows positive temperatures (in phase with solar forcing) that increase in magnitude from the lower to the upper stratosphere, mainly over approximately 40°N–40°S. These results are similar (but of somewhat smaller amplitude) to previous calculations based on the shorter record of SSU alone (Randel et al. 2009). Solar signals derived from recent reanalyses (Mitchell et al. 2014) show a consistent (small) maximum in the tropical lower stratosphere (similar to the MSU4 signal in Fig. 15) but patterns that vary strongly among reanalyses in the upper stratosphere (very different from the strong increase

with altitude in low latitudes seen in SSU + MLS data). The amplitudes and patterns of tropically centered maxima increasing with altitude from the lower to upper stratosphere derived from MSU4 and SSU + MLS data are reasonably consistent with recent chemistry–climate model simulations of the solar cycle shown in Chiodo et al. (2012) and Hood et al. (2015).

The key information from the extended SSU + MLS (or SSU + SABER) data regards long-term changes or trends in stratospheric temperatures. Linear trends calculated from the entire 1979–2015 period show weak annual mean cooling for MSU4 (from -0.1 to $-0.2\,\mathrm{K\,decade^{-1}}$) but strong cooling for the middle and upper stratosphere (from -0.5 to $-0.6\,\mathrm{K\,decade^{-1}}$), with a slight increase in trends with altitude (SSU3 stronger than SSU1). Nearly identical trend results are found between SSU + MLS and SSU + SABER data over 53°N–53°S, while slightly larger cooling is found for SSU2 and SSU3 from SSU + AMSU data. Our global mean trend results for 1979–2015 are somewhat smaller than the trends over 1980–2012 reported in McLandress et al. (2015), but the time periods are different in addition to differences in methodology (we incorporate a multivariate regression model and exclude volcanic periods, which will amplify long-term trends because of warming signals in the early part of the data record). We find good agreement in global trends over 1979–2015 between the SSU + MLS (Table 2) and SSU + AMSU datasets (Zou and Qian 2016). The trends for 1998–2015 are somewhat smaller for SSU + MLS versus SSU + AMSU for the upper-level channels SSU2 and SSU3 but still within statistical uncertainties.

The annual mean SSU trends show a robust latitudinal structure in all of the merged datasets, with relatively constant cooling trends north of about 30°S but weak trends over the high-latitude SH (Fig. 12). The cause of the asymmetric cooling pattern in the middle-to-upper stratosphere (or equivalently, the lack of cooling over Antarctica) is not known. Chemistry–climate model simulations (e.g., Garcia et al. 2007; Stolarski et al. 2010; Marsh et al. 2013) of stratospheric temperature trends during the period of strong halogen-induced ozone losses (~1979–2000) show cooling in the Antarctic lower stratosphere (because of radiative influence of the ozone hole) together with warming over altitudes of approximately 30–50 km (because of changes in stratospheric circulation). It is possible that this behavior is reflected as weak Antarctic trends in the broad-layer SSU temperature trends for the extended period through 2015, although such behavior should be focused primarily in austral spring. The patterns may also reflect low-frequency variations in the stratospheric overturning (Brewer–Dobson) circulation [as discussed, e.g., in Fu et al. (2010, 2015), Young et al. (2012), and Ossó et al. (2015)]. An increased overturning circulation may be supported by the patterns of enhanced low-latitude cooling in the upper stratosphere during SH winter (e.g. Fig. 13d).

Polar temperature variations in the extended SSU + MLS data show the well-known behavior of strong variability during winter–spring (Fig. 14), and no significant trends are found in the 37 years of data during these seasons in either hemisphere. In contrast, the Arctic summer upper stratosphere exhibits strong and highly significant cooling trends (superimposed on very small background variability). Much weaker and marginally significant cooling trends are found in the Antarctic summer upper stratosphere. While not discussed in detail here, the year-to-year variations in winter-spring polar temperatures (e.g., Fig. 14) are reflected in out-of-phase behavior with low latitudes (i.e., north–south seesaw patterns), which is a signature of variability in the Brewer–Dobson circulation (BDC). However, as with the polar temperatures themselves, we find no statistically significant trends in BDC indices [north–south temperature gradients, such as those calculated by Young et al. (2012)] in the SSU + MLS data over 1979–2015.

Model simulations (e.g., Stolarski et al. 2010) suggest that stratospheric temperature changes will evolve in response to changing ozone trends. Satellite measurements show that upper-stratospheric ozone decreased during 1979–97 and increased after 1998 (Bourassa et al. 2014; Kyrölä et al. 2013), likely as a response to changing halogen loading (WMO 2014). Middle-to-upper-stratospheric temperatures from merged SSU + MLS data show strong changes in trends between the periods 1979–97 and 1998–2015 (Fig. 16), with enhanced cooling for the former period (ozone decreases) and weaker cooling for the latter period (ozone increases). The changes in global trends are highly significant between the two periods (Table 2). Together with the observed changes in ozone trends, these evolving temperatures provide unambiguous evidence of stratospheric response to anthropogenic influences.

Acknowledgments. We thank Dian Seidel and Dave Thompson for numerous discussions on stratospheric temperature trends and satellite datasets and Rolando Garcia for comments on the manuscript. Mijeong Park helped provide access to the monthly mean MLS data and produced Fig. 13. Comments from anonymous reviewers led to substantial improvements in the manuscript. This work was partially supported under the NASA *Aura* Science Program. The views, opinions, and

findings contained in this report are those of the authors and should not be construed as an official National Oceanic and Atmospheric Administration or U.S. government position, policy, or decision.

REFERENCES

Bourassa, A. E., D. A. Degenstein, W. J. Randel, J. M. Zawodny, E. Kyrola, C. A. McLinden, C. E. Sioris, and C. Z. Roth, 2014: Trends in stratospheric ozone derived from merged SAGE II and Odin-OSIRIS satellite observations. *Atmos. Chem. Phys.*, **14**, 6983–6994, doi:10.5194/acp-14-6983-2014.

Chen, Y., Y. Han, Q. Liu, P. V. Delst, and F. Weng, 2011: Community radiative transfer model for Stratospheric Sounding Unit. *J. Atmos. Oceanic Technol.*, **28**, 767–778, doi:10.1175/2010JTECHA1509.1.

Chiodo, G., N. Calvo, D. R. Marsh, and R. Garcia-Herrera, 2012: The 11 year solar cycle signal in transient simulations from the Whole Atmosphere Community Climate Model. *J. Geophys. Res.*, **117**, D06109, doi:10.1029/2011JD016393.

Efron, B., and R. J. Tibshirani, 1993: *An Introduction to the Bootstrap*. CRC Press, 436 pp.

Free, M., and J. Lanzante, 2009: Effect of volcanic eruptions on the vertical temperature profile in radiosonde data and climate models. *J. Climate*, **22**, 2925–2939, doi:10.1175/2008JCLI2562.1.

Fu, Q., S. Solomon, and P. Lin, 2010: On the seasonal dependence of tropical lower-stratospheric temperature trends. *Atmos. Chem. Phys.*, **10**, 2643–2653, doi:10.5194/acp-10-2643-2010.

——, P. Lin, S. Solomon, and D. L. Hartmann, 2015: Observational evidence of strengthening of the Brewer–Dobson circulation since 1980. *J. Geophys. Res. Atmos.*, **120**, 10 214–10 228, doi:10.1002/2015JD023657.

Fujiwara, M., T. Hibino, S. K. Mehta, L. Gray, D. Mitchell, and J. Anstey, 2015: Global temperature response to the major volcanic eruptions in multiple reanalysis datasets. *Atmos. Chem. Phys.*, **15**, 13 507–13 518, doi:10.5194/acpd-15-13315-2015.

Garcia, R. R., D. R. Marsh, D. E. Kinnison, B. A. Boville, and F. Sassi, 2007: Simulation of secular trends in the middle atmosphere, 1950–2003. *J. Geophys. Res.*, **112**, D09301, doi:10.1029/2006JD007485.

Harris, N. R. P., and Coauthors, 2015: Past changes in the vertical distribution of ozone—Part 3: Analysis and interpretation of trends. *Atmos. Chem. Phys.*, **15**, 9965–9982, doi:10.5194/acp-15-9965-2015.

Hood, L. L., and Coauthors, 2015: Solar signals in CMIP-5 simulations: The ozone response. *Quart. J. Roy. Meteor. Soc.*, **141**, 2670–2689, doi:10.1002/qj.2553.

Kyrölä, E., M. Laine, V. Sofieva, J. Tamminen, S.-M. Päivärinta, S. Tukiainen, J. Zawodny, and L. Thomason, 2013: Combined SAGE II–GOMOS ozone profile data set for 1984–2011 and trend analysis of the vertical distribution of ozone. *Atmos. Chem. Phys.*, **13**, 10 645–10 658, doi:10.5194/acp-13-10645-2013.

Lee, H., and A. K. Smith, 2003: Simulation of the combined effects of solar cycle, quasi-biennial oscillation, and volcanic forcing on the stratospheric ozone changes in recent decades. *J. Geophys. Res.*, **108**, 4049, doi:10.1029/2001JD001503.

Marsh, D., M. Mills, D. E. Kinnison, and J.-F. Lamarque, 2013: Climate change from 1850 to 2005 simulated in CESM1(WACCM). *J. Climate*, **26**, 7372–7391, doi:10.1175/JCLI-D-12-00558.1.

McLandress, C., T. G. Shepherd, A. I. Jonsson, T. von Clarmann, and B. Funke, 2015: A method for merging nadir-sounding climate records, with an application to the global-mean stratospheric temperature data sets from SSU and AMSU. *Atmos. Chem. Phys.*, **15**, 9271–9284, doi:10.5194/acpd-15-10085-2015.

Mertens, C. J., M. G. Mlynczak, M. Lopez-Puertas, P. P. Wintersteiner, R. H. Picard, J. R. Winick, and L. L. Gordley, 2001: Retrieval of mesospheric and lower thermospheric kinetic temperature from measurements of CO_2 15 μm Earth limb emission under non-LTE conditions. *Geophys. Res. Lett.*, **28**, 1391–1394, doi:10.1029/2000GL012189.

Mitchell, D. M., and Coauthors, 2014: Signatures of naturally induced variability in the atmosphere using multiple reanalysis datasets. *Quart. J. Roy. Meteor. Soc.*, **141**, 2011–2031, doi:10.1002/qj.2492.

Nash, J., and R. Saunders, 2015: A review of Stratospheric Sounding Unit radiance observations for climate trends and reanalyses. *Quart. J. Roy. Meteor. Soc.*, **141**, 2103–2113, doi:10.1002/qj.2505.

Ossó, A., Y. Sola, K. Rosenlof, B. Hassler, J. Bech, and J. Lorente, 2015: How robust are trends in the Brewer–Dobson circulation derived from observed stratospheric temperatures? *J. Climate*, **28**, 3024–3040, doi:10.1175/JCLI-D-14-00295.1.

Ramaswamy, V., and Coauthors, 2001: Stratospheric temperature trends: Observations and model simulations. *Rev. Geophys.*, **39**, 71–122, doi:10.1029/1999RG000065.

Randel, W. J., and F. Wu, 1999: Cooling of the Arctic and Antarctic polar stratosphere due to ozone depletion. *J. Climate*, **12**, 1467–1479, doi:10.1175/1520-0442(1999)012<1467:COTAAA>2.0.CO;2.

——, and Coauthors, 2009: An update of observed stratospheric temperature trends. *J. Geophys. Res.*, **114**, D02107, doi:10.1029/2008JD010421.

Remsberg, E. E., and Coauthors, 2008: Assessment of the quality of the version 1.07 temperature-versus-pressure profiles of the middle atmosphere from *TIMED*/SABER. *J. Geophys. Res.*, **113**, D17101, doi:10.1029/2008JD010013.

Robock, A., 2000: Volcanic eruptions and climate. *Rev. Geophys.*, **38**, 191–219, doi:10.1029/1998RG000054.

Schwartz, M. J., and Coauthors, 2008: Validation of the *Aura* Microwave Limb Sounder temperature and geopotential height measurements. *J. Geophys. Res.*, **113**, D15S11, doi:10.1029/2007JD008783.

Seidel, D. J., N. P. Gillett, J. R. Lanzante, K. P. Shine, and P. W. Thorne, 2011: Stratospheric temperature trends: Our evolving understanding. *Wiley Interdiscip. Rev.: Climate Change*, **2**, 592–616, doi:10.1002/wcc.125.

——, and Coauthors, 2016: Stratospheric temperature changes during the satellite era. *J. Geophys. Res. Atmos.*, **121**, 664–681, doi:10.1002/2015JD024039.

Shine, K. P., and Coauthors, 2003: A comparison of model-predicted trends in stratospheric temperatures. *Quart. J. Roy. Meteor. Soc.*, **129**, 1565–1588, doi:10.1256/qj.02.186.

Stolarski, R. S., A. R. Douglass, P. A. Newman, S. Pawson, and M. R. Schoeberl, 2010: Relative contribution of greenhouse gases and ozone-depleting substances to temperature trends in the stratosphere: A chemistry–climate model study. *J. Climate*, **23**, 28–42, doi:10.1175/2009JCLI2955.1.

Thomason, L. W., and T. Peter, Eds., 2006: Assessment of stratospheric aerosol properties (ASAP). SPARC Rep. 4, WCRP-124, WMO/TD-1295, 321 pp. [Available online at http://www.sparc-climate.org/publications/sparc-reports/sparc-report-no4/.]

Thompson, D. W. J., and Coauthors, 2012: The mystery of recent stratospheric temperature trends. *Nature*, **491**, 692–697, doi:10.1038/nature11579.

Wallace, J. M., R. L. Panetta, and J. Estberg, 1993: Representation of the equatorial stratospheric quasi-biennial oscillation in EOF phase space. *J. Atmos. Sci.*, **50**, 1751–1762, doi:10.1175/1520-0469(1993)050<1751:ROTESQ>2.0.CO;2.

Wang, L., C.-Z. Zou, and H. Qian, 2012: Construction of stratospheric temperature data records from stratospheric sounding units. *J. Climate*, **25**, 2931–2946, doi:10.1175/JCLI-D-11-00350.1.

WMO, 2014: Scientific assessment of ozone depletion: 2014. WMO Global Ozone Research and Monitoring Project Rep. 55, 416 pp. [Available online at http://www.wmo.int/pages/prog/arep/gaw/ozone_2014/documents/Full_report_2014_Ozone_Assessment.pdf.]

Young, P. J., K. H. Rosenlof, S. Solomon, S. C. Sherwood, Q. Fu, and J.-F. Lamarque, 2012: Changes in stratospheric temperatures and their implications for changes in the Brewer–Dobson circulation, 1979–2005. *J. Climate*, **25**, 1759–1772, doi:10.1175/2011JCLI4048.1.

Zou, C.-Z., and H. Qian, 2016: Stratospheric temperature climate data from merged SSU and AMSU-A observations. *J. Atmos. Oceanic Technol.*, in press.

——, ——, W. Wang, L. Wang, and C. Long, 2014: Recalibration and merging of SSU observations for stratospheric temperature trend studies. *J. Geophys. Res. Atmos.*, **119**, 13 180–13 205, doi:10.1002/2014JD021603.